Cell Reports
Physical Science

CellPress
OPEN ACCESS

Article

Modeling and design of III-V heterojunction solar cells for enhanced performance

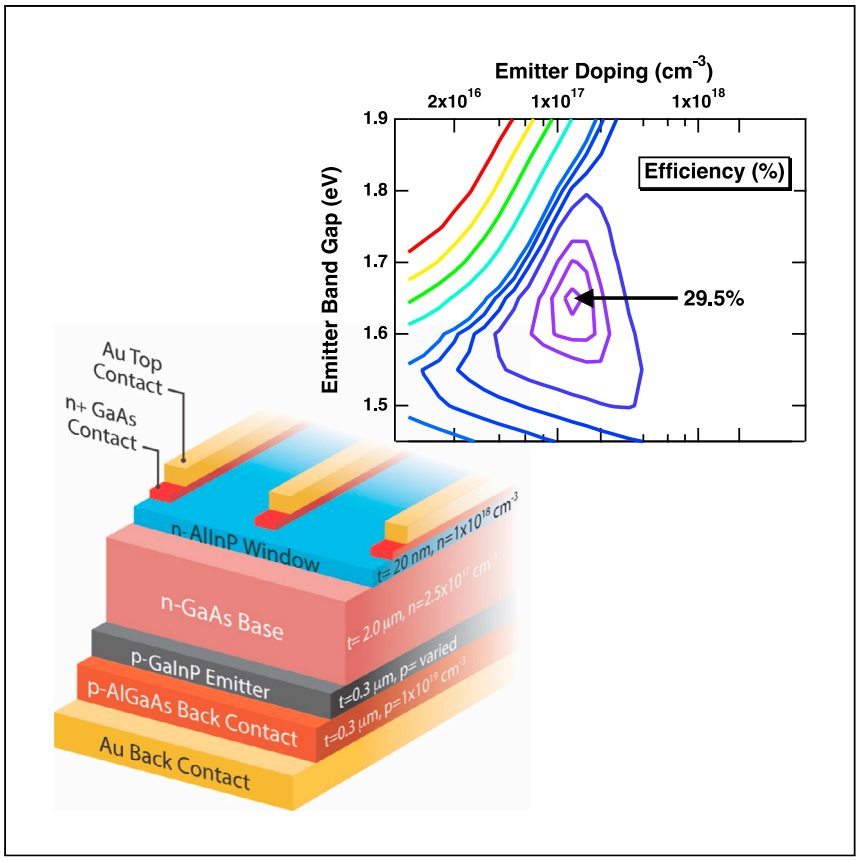

Heterojunction solar cells can enhance solar cell efficiency. Schulte et al. model a rear heterojunction III-V solar cell design comprising a lower band gap absorber and a wider band gap emitter and show that optimization of emitter doping and heterojunction band offsets enhances efficiency. The model predictions are validated experimentally and used to fabricate an HVPE-grown GaAs/GaInPAs solar cell with 27% efficiency, and the model is potentially applicable to other materials systems.

Kevin L. Schulte, John Simon, Myles A. Steiner, Aaron J. Ptak

kevin.schulte@nrel.gov

Highlights

Computational modeling and experimental testing of rear heterojunction solar cells

Efficiency is a function of emitter doping and energy band offsets

Model results inform the development of a 27% efficient GaAs cell grown by HVPE

Model results developed using III-Vs are potentially applicable to other materials

Schulte et al., Cell Reports Physical Science 4, 101541
September 20, 2023
https://doi.org/10.1016/j.xcrp.2023.101541

Cell Reports
Physical Science

CellPress
OPEN ACCESS

Article

Modeling and design of III-V heterojunction solar cells for enhanced performance

Kevin L. Schulte,[1,2,*] John Simon,[1] Myles A. Steiner,[1] and Aaron J. Ptak[1]

SUMMARY

Heterojunctions can increase the efficiency of solar cell devices relative to homojunctions, but there is a large parameter space with significant tradeoffs that must be considered. Here, we present an experimental and computational study of III-V heterojunction solar cells and show how the emitter doping, emitter band gap, and heteroband offsets impact device efficiency. Efficiency is maximized by pushing the junction depletion region into the wider band gap material while minimizing the effects of heteroband offsets through optimized choice of emitter band gap, emitter electron affinity, and/or emitter doping density. We use these results to guide optimization of devices grown by halide vapor phase epitaxy, achieving 27% efficiency in a GaAs/GaInPAs heterojunction device. We also show that heterojunctions yield proportionally larger efficiency improvements in lower-quality materials. Although the modeling was developed and validated using III-V materials, the results are theoretically applicable to materials systems outside III-Vs.

INTRODUCTION

Heterojunctions offer the potential for enhanced efficiency in solar cell devices.[1–3] Device modeling and experiment suggest that shifting a portion of the depletion region formed at a p-n junction into a wider band gap material reduces the Shockley-Read-Hall (SRH) recombination rate. This is clear when considering Sah's derivation of the SRH recombination rate, U, at the boundary of a p-n junction[4]:

$$U(V) = \frac{n_i e^{\frac{qV}{2kT}}}{2\tau_0,} \qquad \text{(Equation 1)}$$

where n_i is the intrinsic carrier concentration, q is the elementary charge, V is the bias voltage, k is Boltzmann's constant, T is the device temperature, and τ_0 is the electron or hole lifetime. n_i is an inverse exponential function of band gap, so the recombination rate and non-radiative SRH dark current density (J_{02}) decrease exponentially with increasing band gap. In turn, a reduction in recombination current increases the open-circuit voltage (V_{OC}) as the device becomes radiative current density (J_{01}) limited and the photovoltaic conversion efficiency of the device increases.[5,6] A rear heterojunction with a low-band gap material on top of a higher-gap material benefits from reduced radiative recombination in the larger band gap material without sacrificing photon absorption. The benefits of heterojunctions are known, although experimental demonstrations of III-V heterojunctions are limited to a handful of combinations with a single emitter doping level, such as GaAs (1.42 eV)/$Ga_{0.51}In_{0.49}P$ (1.85 eV),[7] GaAs/$Ga_{0.7}Al_{0.3}As$ (1.80 eV),[2,8] or $Ga_{0.51}In_{0.49}P$ (1.85 eV)/$Al_{0.25}Ga_{0.25}In_{0.5}P$ (2.22 eV).[1] III-V compositions and band gaps are highly tunable, so there exist other combinations that potentially offer higher efficiency.

[1]National Renewable Energy Laboratory, Golden, CO 80401, USA

[2]Lead contact

*Correspondence: kevin.schulte@nrel.gov

https://doi.org/10.1016/j.xcrp.2023.101541

The heterojunction comprises two layers that we define as the base layer, which is the lower band gap layer responsible for the majority of light absorption and carrier generation, and the emitter, which completes the junction and participates in carrier extraction. Heterojunctions require careful design because the discontinuity of the energy bands at the heterointerface may create barriers that hinder current extraction.[3,9] These heterobarriers can be managed by using a high doping density in the emitter to increase the field in the depletion region and/or enable tunneling, as well as by proper choice of materials combinations targeting those with favorable band offsets.[10] Higher emitter doping requires a tradeoff, however, because non-radiative recombination will increase as the depletion region shifts from the wide band gap emitter into the lower band gap base. Device modeling is an efficient way to study these tradeoffs over a wide parameter space.

Here, we present a computational and experimental study of GaAs rear heterojunction (RHJ) solar cells that use $Ga_xIn_{1-x}P_yAs_{1-y}$ or $Al_xGa_{1-x}As$ emitters. We use the open access solver AFORS-HET,[11] which solves the 1D drift-diffusion equations and Poisson's equation using a finite element method, enabling the computation of current density-voltage (*J-V*) curves under a wide range of conditions. We elucidate the relationships between device performance and emitter doping, emitter band gap, and heterojunction band offset (electron affinity). We show that there is an optimum emitter doping density and band gap to maximize efficiency, and that the size of this optimum varies with the heteroband offsets as defined by the material choice. We use these results to guide optimization of GaAs RHJ solar cells grown by halide vapor phase epitaxy (HVPE), a promising route to lowering the cost of III-V device epitaxy,[12,13] achieving an NREL-certified AM1.5G efficiency of 27% with a GaAs (1.42 eV)/$Ga_{0.68}In_{0.32}P_{0.66}As_{0.34}$ (1.70 eV) combination. We also show that relatively higher efficiency improvements are possible in lower-quality material. These results are theoretically applicable to materials systems outside of III-Vs that employ heterojunctions, such as Si,[14] CdTe,[15] or perovskites,[16] in the limit that non-radiative SRH recombination limits their efficiency.

RESULTS AND DISCUSSION

Effect of emitter doping

We first tested the model using the commonly employed n-GaAs (1.42 eV)/p-$Ga_{0.51}In_{0.49}P$ (1.85 eV) RHJ structure. We studied a series of RHJ solar cells grown by organometallic vapor phase epitaxy (OMVPE) with variable doping in the p-type $Ga_{0.51}In_{0.49}P$ emitter and compared the experimentally measured device characteristics to model predictions. Figure 1A shows the device structure. The GaAs/$Ga_{0.51}In_{0.49}P$ junction has a ~370 mV heterobarrier in the valence band[17,18] that was shown to decrease current collection at homo-doped interfaces if the GaInP doping is not sufficiently high.[10,19] Similarly, this barrier greatly impacts current collection in a p-n heterojunction, as well. Figure 1B shows light *J-V* curves for five devices with $Ga_{0.51}In_{0.49}P$ emitter doping (p) between 9×10^{15} cm^{-3} and 8.0×10^{17} cm^{-3}. The fill factor (FF) of the experimentally measured curves, listed in the figure, and short-circuit current density (J_{SC}) decrease strongly with decreasing p until there is minimal photo-generated current collection in the device with the lowest emitter doping. Figure 1C presents energy band calculations of the devices with $p = 1.3 \times 10^{17}$ cm^{-3} and $p = 8.0 \times 10^{17}$ cm^{-3} under conditions of 0.95 V forward bias (indicated by the vertical broken line in Figure 1B) and AM1.5G illumination. The non-radiative recombination rate of carriers predicted by the model is plotted as broken curves on the mirror y axis of this graph. Looking at the energy band plots, the reduced doping density lowers the field strength near the junction, seen in the

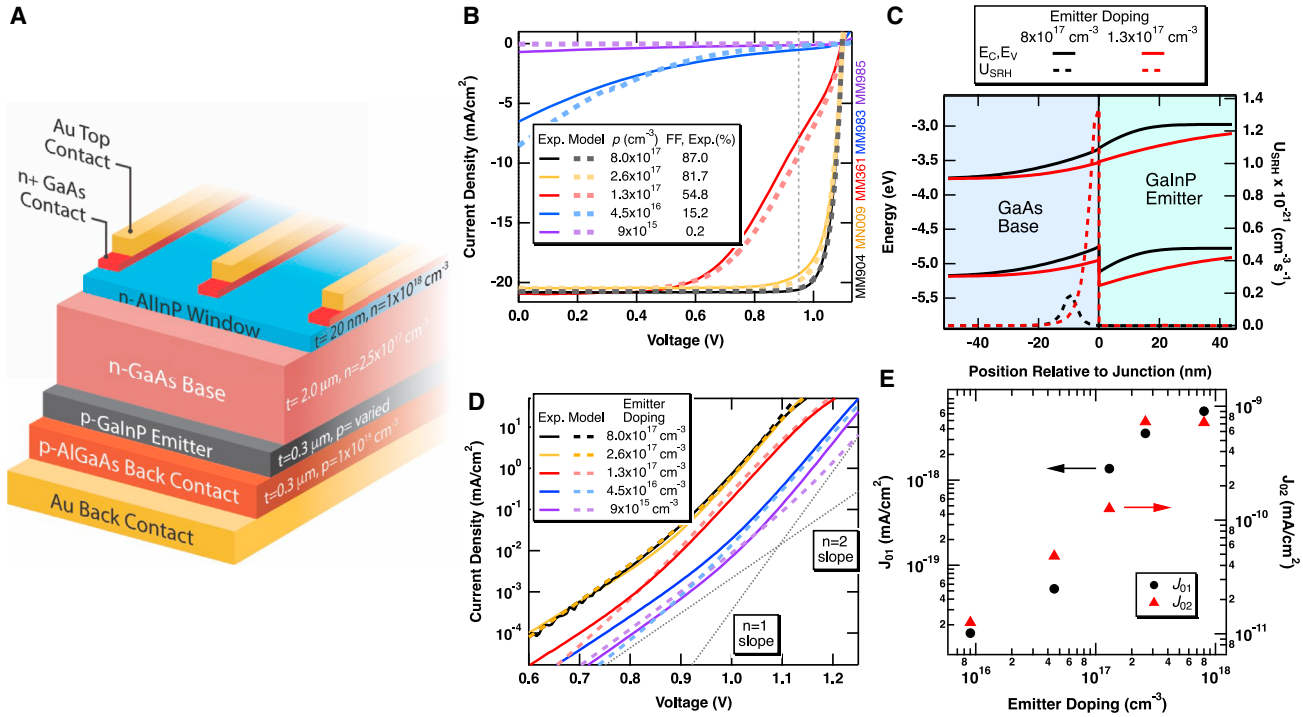

Figure 1. Modeling of GaAs/GaInP rear heterojunction devices

(A) Schematic of the simulated and experimentally realized GaAs/GaInP rear heterojunction devices. The doping density of the GaInP emitter was varied with all other parameters remaining constant.

(B) Measured and simulated light *J-V* curves under the AM1.5G spectrum for devices with varying emitter doping density.

(C) Calculated energy band diagram focused on the GaAs/GaInP heterointerface. The SRH recombination rate is plotted as a function of position on the right axis as the broken lines.

(D) Measured and simulated dark *J-V* curves for the devices. The dotted lines indicate the idealized *J-V* slope of a device limited by J_{01} or J_{02} dark current.

(E) J_{01} and J_{02} derived from fitting the experimental dark *J-V*s shown in (D) plotted as a function of the GaInP emitter doping density.

more moderate slope in the band energies, which limits the ability of holes generated in the GaAs base to flow across the heterojunction into the emitter due to the large valence band offset. The buildup of holes at the interface leads to an elevated non-radiative recombination rate of carriers in the base of the lower doped device relative to the higher doped device. This effect reduces the useful current generated by the device, causing the severe drop in *FF* with doping observed in the light *J-V* curves. Figure 1B also compares the model-calculated light *J-V* curves to the experimental data. The close agreement over a wide range of doping suggests that the device model captures the relevant physics controlling the performance of these rear heterojunction devices. Figure 1D shows the measured and calculated dark *J-V* curves, along with guides to the eye for the slope of diodes limited by J_{01} (n = 1) or J_{02} (n = 2) recombination current. Figure 1E plots J_{01} and J_{02} derived from fitting the experimental dark *J-V* curves to a two-diode model[20] as a function of emitter doping. The dark *J-V* curves do not change much with p from $p = 8.0 \times 10^{17}$ cm^{-3} to $p = 2.6 \times 10^{17}$ cm^{-3}, but there is a marked reduction in the J_{02} dark current as the doping density decreases below that of the GaAs base ($n \sim 2.5 \times 10^{17}$ cm^{-3}), and the majority of the depletion width moves into the wide band gap $Ga_{0.51}In_{0.49}P$ emitter (see Figure S1 for estimates of the depletion in each layer as a function of doping and band gap). We attribute the decrease in J_{02} to reduced non-radiative recombination at traps in the depletion region. J_{01} also

decreases somewhat at that doping level. J_{01} and J_{02} both drop strongly with further decreases in emitter doping. We attribute the reduction in J_{01} with doping to reduced hole injection across the junction because of the presence of the barrier, which reduces the diffusive J_{01} recombination current in the GaAs base. Normally, these significant reductions in dark current might be expected to lead to increased V_{OC}, based on the principle of superposition of light and dark *J-V*s,[21] but the V_{OC}s obtained in the light in Figure 1B are relatively constant with emitter doping. The V_{OC}s are similar because recombination rates in these RHJ devices are dominated by the hole population in the n-GaAs base. While this varies with emitter doping in the dark due to reduced injection across the barrier at low doping, the base's hole concentration in the light is dominated by photo-generation, which is constant in this sample set because they have the same structure and layer thicknesses. Thus, superposition of the light and dark *J-V*s breaks down at low emitter doping, and the potential efficiency gain is limited to the reduction in J_{02}, which was already low in these devices due to a low trap density (see experimental procedures). Overall, the agreement between the model and the experiment is quite good, although we note some small differences that may be related to assumptions of the model, which ignored effects of surface and interface recombination.

Effect of band offset

$Ga_{0.51}In_{0.49}P$ provides reasonably good performance as an emitter; however, its use requires doping of $p \sim 1 \times 10^{18}$ cm^{-3} or greater to mitigate the effects of the heterobarrier described above. This doping level precludes any potential benefit from moving the depletion into this wider band gap layer. The ability to tune the band offset is desirable, but the offset is a fixed property of a given base/emitter materials combination. We can modify the GaInP composition by adding arsenic to form the quaternary alloy $Ga_xIn_{1-x}P_yAs_{1-y}$ that provides a tunable set of compositions with band gaps between GaAs (1.42 eV) and GaInP (1.9 eV). The GaAs/$Ga_xIn_{1-x}P_yAs_{1-y}$ valence band offset is a linear function of the band gap for compositions lattice-matched to GaAs,[18,22] meaning that we can tune the band offset by varying the composition. To study the effect of varying the valence band offset in this way, we modeled GaAs/$Ga_xIn_{1-x}P_yAs_{1-y}$ devices with varying emitter doping and composition, with the constraint of lattice-matching of the $Ga_xIn_{1-x}P_yAs_{1-y}$ to the GaAs lattice constant, and we tested the model using HVPE-grown RHJ devices. We assumed a trap concentration $N_T = 1.3 \times 10^{14}$ cm^{-3} of the "EL2" or As anti-site defect (see experimental procedures for more details of the defect model) in both the GaAs layer and $Ga_xIn_{1-x}P_yAs_{1-y}$ emitter, representing the demonstrated quality of our HVPE-grown material.[23] Figures 2A–2D show contour maps of the simulated V_{OC}, J_{SC}, *FF*, and photovoltaic conversion efficiency as a function of emitter band gap and doping density under a one-sun AM1.5G illumination condition. Note that surface reflectance and series resistance are both assumed to be zero in these calculations. Looking at V_{OC}, we see that that there is an optimum at a band gap of ~1.8 eV and $p \sim 5 \times 10^{16}$ cm^{-3}. Compared to a hypothetical baseline standard structure indicated by the green dot (1.85 eV $Ga_{0.51}In_{0.49}P$ emitter, $p = 1 \times 10^{18}$ cm^{-3}), V_{OC} increases initially with decreasing emitter doping due to the depletion region being pushed further into the wide band gap emitter (see Figure S1), which minimizes the contribution of the J_{02} current to the total dark current. As an aside, we note that there is no optimum V_{OC} for perfect materials because that parameter continually increases with emitter band gap and doping (see Figure S2). Past the maximum, V_{OC} decreases with further decrease in emitter doping because the total depletion width expands rapidly, while the amount in the GaAs base stays relatively constant, increasing J_{02}, although this effect is quite small. The maximum in *V*oc does not coincide with the optimum in efficiency, however. The J_{SC} is relatively

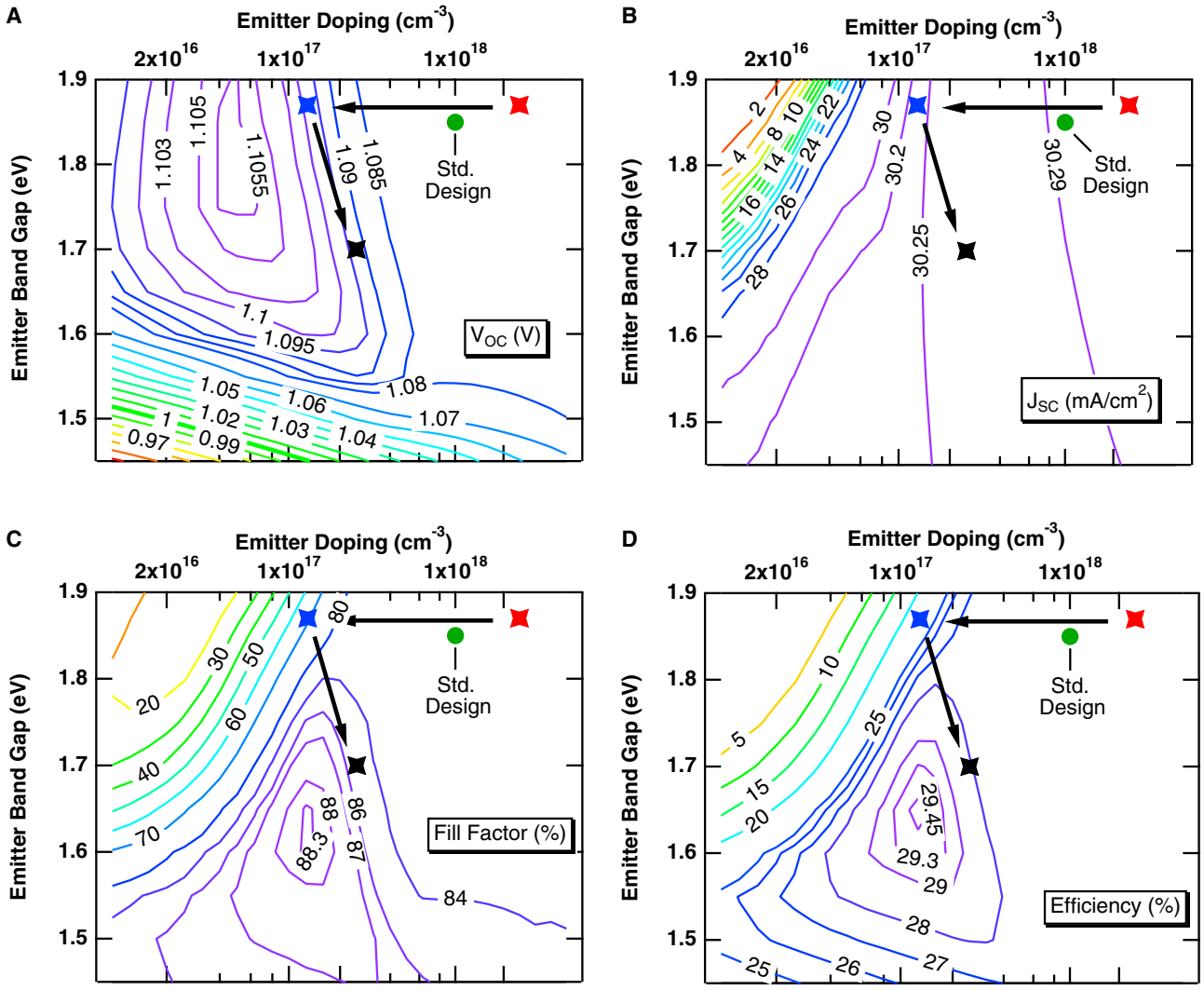

Figure 2. Simulated solar cell parameters for GaAs/$Ga_xIn_{1-x}P_yAs_{1-y}$ rear heterojunction solar cells as a function of emitter band gap and doping density

V_{OC} (A), J_{SC} (B), *FF* (C), and efficiency (D). A deep level trap density of $N_T = 1.3 \times 10^{14}$ was assumed in the emitter and base. The stars indicate the predicted metrics for the HVPE-grown devices shown in Figure 3. Note that the model assumes no reflectance at the front surface or resistance in the electrical contacts.

constant for an emitter band gap below 1.65 eV and/or $p \geq 6 \times 10^{17}$ cm^{-3}, but the *FF* and efficiency show a steep contour with a peak at 1.65 eV and $p = 1.3 \times 10^{17}$ cm^{-3}. The optimum in *FF* occurs because J_{02} decreases with doping, which increases *FF*, but *FF* decreases when the doping becomes too low and the heterobarrier limits photocurrent collection (as observed experimentally in Figure 1B). Reducing the emitter band gap, and by extension, the heterobarrier height, at constant doping mitigates this problem. However, there is also an optimum with emitter band gap because J_{02} increases as the band gap is reduced (see Equation 1) minimizing the benefit of placing the depletion region there. Comparing the positions of the optima in the *FF* and efficiency graphs shows that maximizing the *FF* is key to high efficiency.

These results show that the baseline RHJ design ($Ga_{0.51}In_{0.49}P$ emitter, $p = 1 \times 10^{18}$ cm^{-3}), with a predicted efficiency of 27.4%, is not the most efficient design.

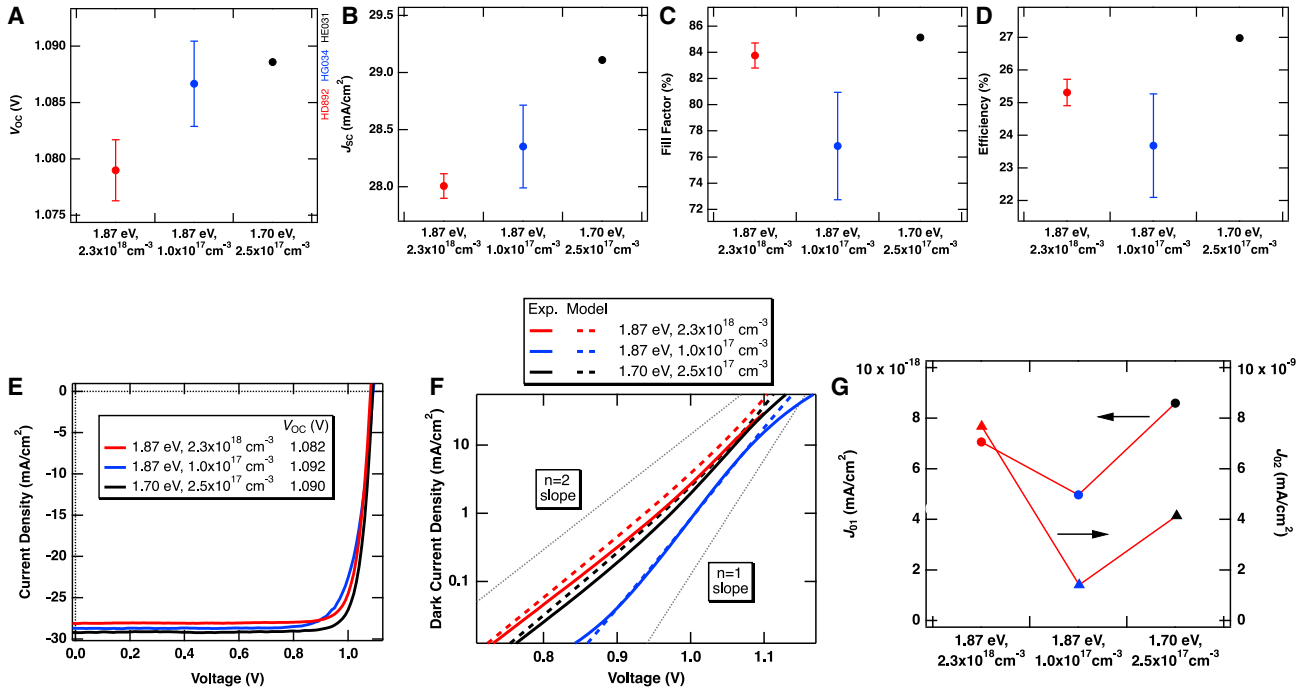

Figure 3. Model-guided optimization of HVPE-grown GaAs/$Ga_xIn_{1-x}P_yAs_{1-y}$ devices

(A–D) V_{OC} (A), J_{SC} (B), *FF* (C), and efficiency (D) for HVPE-grown RHJ solar cells with varied emitter band gap and doping density. These devices employ anti-reflection coatings. The error bars are the standard deviation of six devices.

(E) Measured light *J-V* curves for select devices.

(F) Measured and simulated dark *J-V* curves for select devices.

(G) J_{01} and J_{02} derived from fitting the experimental dark *J-V*s shown in (F).

Efficiency increases with lower values of emitter band gap and doping density, reaching 29.4% with an emitter band gap of 1.65 eV and $p = 1.3 \times 10^{17}$ cm^{-3}. This is a 2% absolute and 7% relative efficiency increase obtained simply by changing the device design to minimize J_{02} while managing the impact of the heterobarrier and making no improvements to material quality. We note that this efficiency is not a global maximum, as the choice of an emitter from a materials system with even better heteroband alignment could allow higher efficiency (as we will show later).

Next, we used the model results to guide the optimization of our HVPE-grown GaAs rear heterojunction solar cells and verify the model predictions. We grew a baseline HVPE structure using a $Ga_{0.51}In_{0.49}P$ emitter with a band gap of 1.87 eV and an emitter doping of 3×10^{18} cm^{-3}, signified by the red star in Figures 2A–2D. This structure is the same as in Figure 1A with a GaInP window instead of AlInP and the addition of a ZnS/MgF_2 anti-reflection coating. Figures 3A–3D (red points) show the V_{OC}, J_{SC}, *FF*, and conversion efficiency averaged over six of these 0.25 cm^2 devices, Figures 3E and 3F show select light and dark *J-V* curves, respectively, for one of these devices in red, and Figure 3G shows the J_{01} and J_{02} reverse saturation currents extracted from fitting of the dark *J-V*s. Figure 3F also shows the model-calculated dark *J-V*. The device parameters and light and dark *J-V* curves agree nicely with the model predictions. We note that the real *FF* is somewhat lower than the prediction due to series resistance, likely from the front contacts, which was neglected in the model calculation, and that the J_{SC} is slightly lower than predicted because this device used a GaInP window layer instead of the modeled AlInP.[24] Starting with this baseline, we reduced the doping in this cell structure to $p = 1.3 \times 10^{17}$ cm^{-3} (blue

stars in Figure 2 and blue points and curves in Figure 3), which led to an average increase of 8 mV in the V_{OC} over six devices. The V_{OC} increased because of a reduction in J_{02} dark current as shown in Figure 3G and observed in the blue experimental and model dark *J-V* curves of Figure 3F. The overall efficiency of this device structure decreased, however, due to a drop in average *FF* from 83.8% down to 76.8% (see Figure 3C), as predicted by the model and as shown in Figure 2C. We then grew an RHJ with a ~1.70 eV $Ga_{0.68}In_{0.32}P_{0.66}As_{0.34}$[25] emitter that had a doping density of 2.5 × 10^{17} cm^{-2} (black stars in Figure 2) to recover the *FF* by decreasing the valence band heterobarrier height. We note that difficulties during processing led to only one device surviving. This more optimal device structure increased the *FF* to 85.1%, thanks to the reduced heterobarrier offset, and efficiency to 27.0% (black points and curves in Figure 3) as certified by NREL's Cell and Module Performance Team (see Figure S3). The V_{OC} is roughly equal to that of the sample with the GaInP emitter and p = 1.3 × 10^{17} cm^{-3} (blue points and curves), despite the significantly lower dark current observed in that sample in Figure 3F. We observed a similar effect in the sample set of Figure 1, whereby J_{01} and J_{02} decreased steadily with emitter doping, but V_{OC} remained roughly fixed. We note that the GaAs/$Ga_{0.68}In_{0.32}P_{0.66}As_{0.34}$ device has an AlInP window, which explains the slight increase in the J_{SC} to over 29.0 mA/cm^3. This J_{SC} value is equal to our previously reported HVPE-grown GaAs/$Ga_{0.51}In_{0.49}P$ RHJ with an AlInP window,[24] but the increased V_{OC} from the emitter optimization results in a 1% absolute efficiency increase relative to that device. We note that the performance variations in these HVPE cells are consistent with the predictions from the device model, providing further validation for the model.

Effect of material quality

Heterojunctions yield even stronger improvement to devices made from lower-quality material due to the higher non-radiative recombination current. To show this, we modeled GaAs/$Ga_xIn_{1-x}P_yAs_{1-y}$ RHJs with an EL2 defect density of N_T = 1.3 × 10^{15} cm^{-3} in the base and emitter, a 10× increase in defect density relative to the previous section. Figures 4A–4D plots contour maps of the V_{OC}, J_{SC}, FF, and efficiency as a function of emitter band gap and doping density for these devices. All four solar cell device metrics are degraded relative to those shown in Figure 2, but the trends with emitter band gap and doping density are the same. The baseline RHJ (GaInP emitter, p = 1 × 10^{18} cm^{-3} doping) has an efficiency of 20.1%, which increases to 22.9% for a $Ga_xIn_{1-x}P_yAs_{1-y}$ emitter with a band gap of 1.65 eV and p = 1.3 × 10^{17} cm^{-3}. This is a 2.8% absolute and 13.9% relative increase in efficiency obtained in this lower-quality material by simply changing the device design. The relative increase in efficiency is nearly two times larger than for the higher-quality material, demonstrating that the heterojunction design is particularly effective at maximizing efficiency in devices using lower-quality material. This result stems from the fact that the recombination rate is still relatively low in the wider band gap material, even if the emitter has an equal number of defects as the base (as assumed here).

Varying the materials choice of the emitter

The results in the previous sections highlight the effect of the heteroband offsets on RHJ efficiency. Those results considered the $Ga_xIn_{1-x}P_yAs_{1-y}$ alloy system for the emitter, but $Al_xGa_{1-x}As$ is another III-V alloy system that is used as an emitter material in high-efficiency GaAs solar cells.[2,8] $Al_xGa_{1-x}As$ has more favorable valence band offsets compared to $Ga_xIn_{1-x}P_yAs_{1-y}$, although its use is sometimes avoided because it is prone to oxygen contamination.[26] The valence band offset is only ~210 meV[27,28] for a band gap of 1.9 eV ($Al_{0.38}Ga_{0.62}As$), compared to ~370 meV for $Ga_{0.51}In_{0.49}P$. The reduced offset means that it should be easier for hole current to flow across the

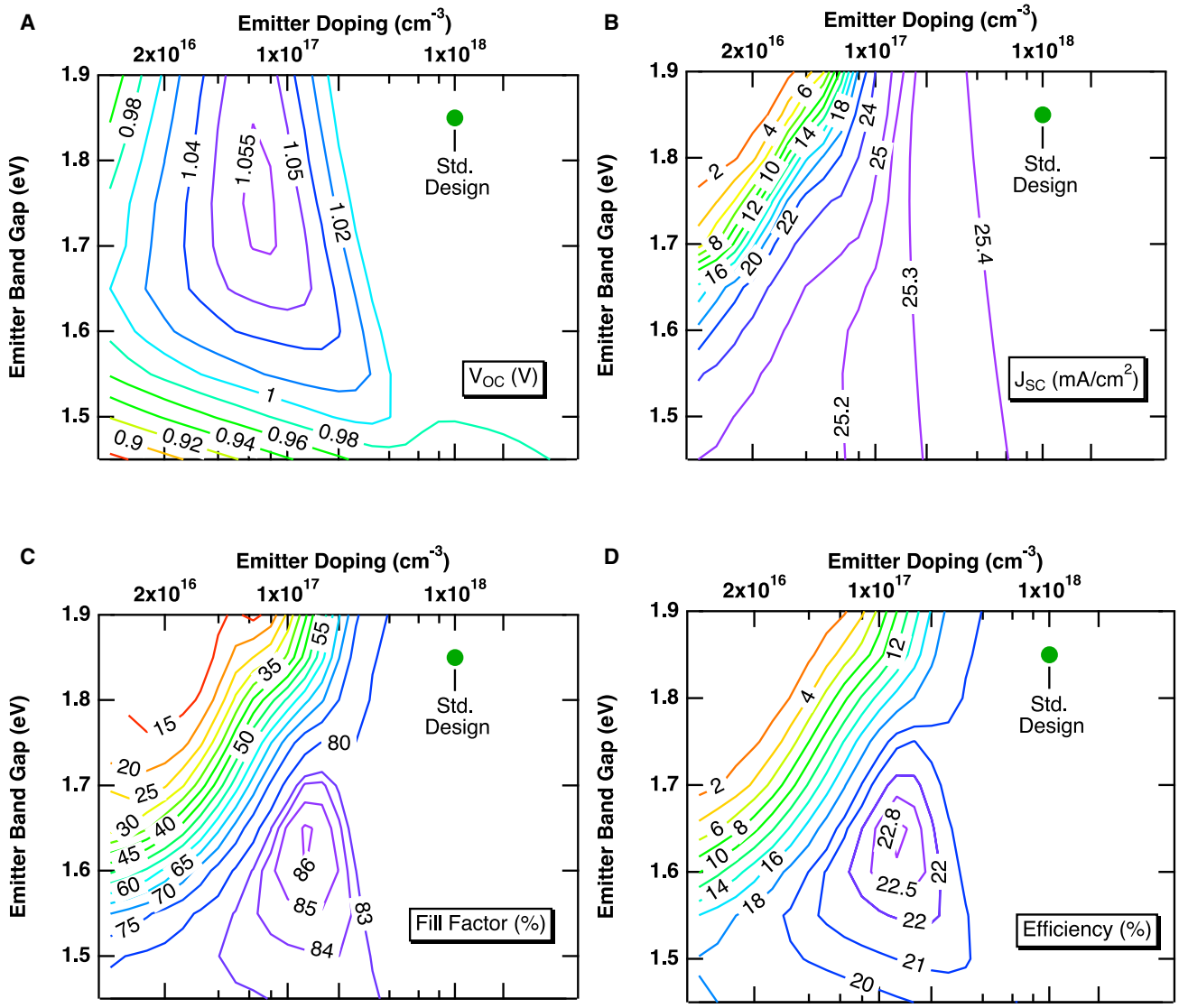

Figure 4. Simulated solar cell parameters for GaAs/$Ga_xIn_{1-x}P_yAs_{1-y}$ rear heterojunctions with reduced material quality

V_{OC} (A), J_{SC} (B), *FF* (C), and efficiency (D) for GaAs/$Ga_xIn_{1-x}P_yAs_{1-y}$ devices with a trap density of $N_T = 1.3 \times 10^{15}$ in the emitter and base, a 10× increase from the devices simulated in Figure 2.

heterointerface, which will manifest as increased *FF* relative to a device with a $Ga_xIn_{1-x}P_yAs_{1-y}$ emitter with the same band gap and doping density. Figures 5A–5D plots contour maps of the V_{OC}, J_{SC}, *FF*, and efficiency as a function of emitter band gap and doping for GaAs/$Al_xGa_{1-x}As$ RHJs. The trap density is again set at the higher value of $N_T = 1.3 \times 10^{15}$ cm^{-3} in the base and emitter, making these calculations directly comparable to those in Figure 4.

The peak V_{OC} and J_{SC} shown in Figure 5 are roughly the same magnitude as in Figure 4, because the material quality is the same, but there are some notable differences in other parameters compared to the $Ga_xIn_{1-x}P_yAs_{1-y}$ emitter case. First, the maxima in *FF* and efficiency for heterojunctions with $Al_xGa_{1-x}As$ are shifted up in band gap to 1.75 eV vs. 1.65 eV because the reduced heteroband offset decreases the penalty paid in reduced *FF* for using a wider band gap emitter. The *FF* and

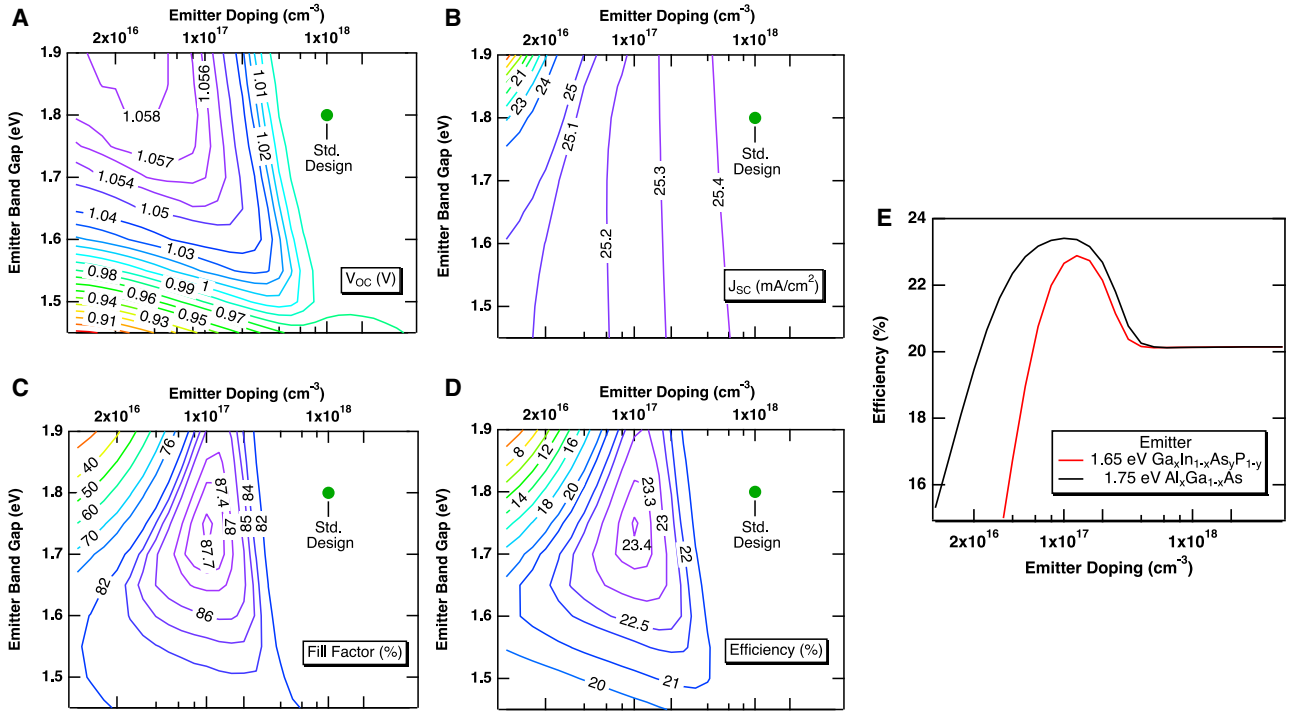

Figure 5. Simulated solar cell parameters for GaAs/$Al_xGa_{1-x}As$ rear heterojunctions with reduced material quality

(A–D) V_{OC} (A), J_{SC} (B), *FF* (C), and efficiency (D) for GaAs/$Al_xGa_{1-x}As$ devices. The trap density is $N_T = 1.3 \times 10^{15}$ in the emitter and base, the same density used in Figure 4.

(E) Line cut of simulated efficiency vs. emitter doping for GaAs/$Ga_xIn_{1-x}P_yAs_{1-y}$ and GaAs/$Al_xGa_{1-x}As$ devices. Each line cut passes through the maximum in efficiency of the contour plots in Figures 4D and 5D.

efficiency peak occur at a slightly lower doping of $p = 1.0 \times 10^{17}$ cm^{-3} for this reason as well. The ability to use a wider band gap emitter than in the $Ga_xIn_{1-x}P_yAs_{1-y}$ case results in an increased peak efficiency compared to that case, 23.4% vs. 22.9%. Comparing again to a baseline design (1.8 eV $Al_{0.3}Ga_{0.7}As$ emitter, $p = 1.0 \times 10^{18}$ cm^{-3} doping density), using the optimum emitter band gap and doping yields a 3.3% absolute and 16.4% relative increase in efficiency. This increase is significantly larger than possible in the $Ga_xIn_{1-x}P_yAs_{1-y}$ emitter devices, enabled by choosing an emitter material with a more favorable heteroband offset. Another point to note is that the drop-off in *FF* (and by extension, efficiency) with decreasing doping density for a given band gap is much less steep compared to the $Ga_xIn_{1-x}P_yAs_{1-y}$ emitter case because of the reduced heteroband offset. This is highlighted in Figure 5E, which plots a line cut of efficiency as a function of doping density for both emitter materials that passes through the maximum efficiency for each case. It is apparent that the efficiency drop-off at lower doping values is less steep when using $Al_xGa_{1-x}As$. Thus, the efficiency of the GaAs/$Al_xGa_{1-x}As$ RHJ is less susceptible to fluctuations in doping and emitter band gap compared to the GaAs/$Ga_xIn_{1-x}P_yAs_{1-y}$ case. In other words, GaAs/$Al_xGa_{1-x}As$ has a more forgiving design window for achieving high efficiency, thanks to the more favorable heteroband offsets.

In summary, we used a combination of device modeling and experiment to demonstrate the benefits of using heterojunctions in III-V solar cells and to explore the tradeoffs that must be considered in their design. The key factor is to push most of the depletion width into the wide band gap material, minimizing the J_{02} dark current, thereby increasing V_{OC} and *FF*, and by extension, efficiency. The modeling

highlighted that particular attention must be paid to managing the heterobarriers to current flow at the junction interface. We used the predictions of the modeling to optimize HVPE-grown GaAs/$Ga_xIn_{1-x}P_yAs_{1-y}$ rear heterojunction solar cells, achieving an efficiency of 27% under a one-sun AM1.5G spectrum in a device with a 1.7 eV $Ga_{0.68}In_{0.32}P_{0.66}As_{0.34}$ emitter. We showed that heterobarriers can be mitigated by reducing the emitter band gap in a given alloy system or choosing entirely different alloys with more favorable offsets, as in the case of GaAs/$Al_xGa_{1-x}As$ vs. GaAs/$Ga_xIn_{1-x}P_yAs_{1-y}$. We showed that a heterojunction device design can be even more impactful in materials that have a high level of defects due to their ability to strongly reduce J_{02}. We note that, while we used III-V materials in the modeling and in experimental device validation, these results are agnostic to material type as long as SRH recombination is the dominant recombination mechanism.

EXPERIMENTAL PROCEDURES

Resource availability

Lead contact

Further information and requests for resources should be directed to and will be fulfilled by the lead contact, Kevin Schulte (kevin.schulte@nrel.gov).

Materials availability

This study did not generate new unique reagents.

Data and code availability

The optical parameters used in the simulation are provided in Data S2. Other data generated from this study are available from the authors upon reasonable request. This paper does not report original code.

Device modeling

Device modeling was conducted using the open access software package AFORS-HET,[11] which solves the 1D drift-diffusion device equations and Poisson's equation using a finite element method. The modeled device structure consisted of four layers: 20 nm $Al_{0.53}In_{0.47}P$ window, 2.0 μm GaAs emitter, 300 nm $Ga_xIn_{1-x}P_yAs_{1-y}$ or $Al_xGa_{1-x}As$ emitter, and 300 nm $Al_{0.35}Ga_{0.65}As$ back contact. The device was discretized in 1D into a 368-point grid, with grids concentrated especially at the interfaces between layers. The material parameters used in the model are listed in Table 1. ε is the low-frequency dielectric constant, χ is the electron affinity, E_G is the band gap, N_C is the conduction band density of states, N_V is the valence band density of states, μ_n is the electron mobility, μ_p is the hole mobility, N_A is the acceptor doping density in the emitter, N_D is the donor doping density in the base, v_n is the electron velocity, v_p is the hole velocity, and B is the radiative recombination coefficient. We assumed a constant doping density within a given layer, abrupt heterointerfaces with no intermixing, and neglected any possible interface recombination. The device temperature was set as 298 K. The effects of series resistance from contacts or sheet resistance were not considered in the modeling. An AM1.5G spectrum was used for simulated light *J-V* calculations. Absorption was determined using a Beer-Lambert model that accounted for a second pass of light from reflectance off the back surface. The reflectance at the back surface was set at 93%.[7] n and k data for representative AlInP, GaAs, AlGaAs, and GaInP layers were measured using spectroscopic ellipsometry and are available in Data S2.

The effects of photon recycling were not treated explicitly but were instead treated as a reduction of the radiative recombination coefficient. Analogously, photon recycling led to an apparent decrease in this parameter in time-resolved

Table 1. Parameters used in the device model

	n-AlInP window	n-GaAs base	*p*-$Ga_xIn_{1x}As_yP_{1-y}$ emitter	*p*-AlGaAs emitter	*p*-AlGaAs contact
Thickness (nm)	20	2,000	300	300	300
ε	11.9	12.9	11.8	12.8–11.8	11.8
χ (eV)	3.78	4.07	4.052–3.960	4.053–3.802	3.802
E_G (eV)	2.248	1.42	1.45–1.9	1.45–1.9	1.9
N_C (cm^{-3})	1.0×10^{18}	4.7×10^{17}	6.5×10^{17}	4.9×10^{17}–8.7×10^{17}	8.7×10^{17}
N_V (cm^{-3})	1.5×10^{18}	9.0×10^{18}	4.3×10^{18}	8.9×10^{18}–6.7×10^{18}	6.7×10^{18}
μ_n ($cm^2\ V^{-1}\ s^{-1}$)	200	4,000	700	600	900
μ_p ($cm^2\ V^{-1}\ s^{-1}$)	30	200	30	70	70
N_A (cm^{-3})	–	–	1.0×10^{16}–5.0×10^{18}	1.0×10^{16}–5.0×10^{18}	1.0×10^{19}
N_D (cm^{-3})	1.0×10^{18}	2.5×10^{17}	–	–	–
v_e ($cm\ s^{-1}$)	1.0×10^{7}	4.4×10^{7}	4.4×10^{7}	3.4×10^{7}	3.4×10^{7}
v_p ($cm\ s^{-1}$)	1.0×10^{7}	1.8×10^{7}	1.8×10^{7}	1.6×10^{7}	1.6×10^{7}
B ($cm^3\ s^{-1}$)	1.0×10^{-10}	3.9×10^{-11} or 1.9×10^{-10}	1.0×10^{-10}	2.4×10^{-10}	2.4×10^{-10}

Sources:[7,17,18,22,27,28,29–32]

photoluminescence measurements of high-quality AlGaAs/GaAs/AlGaAs heterostructures.[33] We estimate B in a device with a gold reflector, B_{Au}, by assuming $B \sim 1 - n_{int}P_{Abs}$, where n_{int} is the internal radiative efficiency of the GaAs absorber, and $\overline{P_{Abs}}$ is the averaged absorption probability for a given photon.[34] For a device left on wafer, $\overline{P_{Abs}}$ was calculated previously to be 0.71, whereas for as a cell with an Au back reflector, $\overline{P_{Abs}}$ was determined to be ~0.97,[7] and n_{int} was 0.965.[34] B was measured to be 1.9×10^{-10} cm3 s^{-1} for an on-wafer sample, and so

$$B_{Au} = 1.9 \times 10^{-10}\ cm^3 s^{-1}\left(\frac{1 - 0.965 * 0.97}{1 - 0.965 * 0.71}\right) = 3.9 \times 10^{-11} cm^3 s^{-1}$$

This is a good estimate for B_{Au} because the V_{OC}s of the cells shown in Figure 1, which are predominantly limited by radiative recombination, are accurately predicted by the model. This reduced value for B was applied to the modeling of the low defect cells in Figures 1, 2, and 3. We assumed the effect of photon recycling is minimal in high defect cells, and we applied the reduced on-wafer value of $B = 1.9 \times 10^{-10}$ cm3 s^{-1} to the modeling of those cells in Figures 4 and 5.

The software uses SRH statistics to compute non-radiative recombination rates in the quasi-neutral and space charge regions. We assumed that the electron trap known as "EL2" is the dominant defect in GaAs and was the only one included in the model. EL2 is a mid-gap defect related to an As anti-site, 0.82 eV below the conduction band, and commonly found in GaAs grown by OMVPE and HVPE.[23,35,36] EL2 is also a dominant trap in OMVPE-grown $Al_xGa_{1-x}As$[37,38] and was modeled as the only defect in that material. In $Al_xGa_{1-x}As$, the trap exhibits a constant position of 0.82 eV below the conduction band even as the Al fraction and band gap vary.[37] Deep traps are less well characterized in $Ga_xIn_{1-x}P_yAs_{1-y}$, but we note a similar electron trap was correlated with group V overpressure in $Ga_{0.51}In_{0.49}P$ grown by multiple groups, suggesting a P anti-site defect that we applied to the model.[39–41] The energy of this defect was also found to be ~0.82 eV below the conduction band. Proper values for the GaAs electron and hole capture cross-sections (σ_n and σ_p) were more difficult to determine. The commonly reported values[42] of σ_n did not cause enough recombination in the model to replicate the observed changes in V_{OC}. However, capture cross-sections can vary up to 1×10^{-12} cm^2 in the presence of an electric field.[43,44] Naturally, in a solar cell, a large majority of SRH recombination happens to occur in the depletion region of a p-n junction where the field is high, so we used larger values for the capture cross-sections. We found that the values of $\sigma_n = 1 \times 10^{-12}$ cm^2 and $\sigma_p = 1 \times 10^{-15}$ cm^2 reproduce the experimental behavior.

These values were also applied to the $Ga_xIn_{1-x}P_yAs_{1-y}$ and $Al_xGa_{1-x}As$ layers. A trap density of $N_T = 2.0 \times 10^{13}$ cm^{-3} was used for the modeling of OMVPE-grown devices shown in Figure 1, $N_T = 1.3 \times 10^{14}$ cm^{-3} in the modeling of HVPE devices in Figures 2 and 3, and $N_T = 1.3 \times 10^{15}$ cm^{-3} in Figures 4 and 5.

Solar cell growth and processing

Solar cells were grown by either HVPE or OMVPE as noted in the results section. See Boyer et al.[24] for HVPE growth details and Steiner et al.[7] for OMVPE growth details. Devices were grown in an inverted fashion, with a GaAs buffer and $Ga_{0.51}In_{0.49}P$ etch stop layer grown first on a GaAs substrate. Devices utilized a GaAs:Se (HVPE) or GaInNAs:Se (OMVPE) front contact grown next, followed by an $Al_{0.53}In_{0.47}P$:Se (or $Ga_{0.51}In_{0.49}P$:Se where noted) window, GaAs:Se base doped to 2–3 x 10^{17} cm^3, $Ga_{0.51}In_{0.49}P$:Zn or $Ga_{0.68}In_{0.32}P_{0.66}As_{0.34}$:Zn emitter, and AlGaAs:Zn (HVPE) or AlGaAs:C (OMVPE) back contact. For processing, a reflective Au metal contact was electroplated onto the AlGaAs contact layer, and then samples were inverted onto an Si handle, and the substrate was etched away followed by the etch stop. For the HVPE devices, Ni/Au grids with 2% area coverage were defined by photolithography and electroplated onto the front surface. 0.25-cm^2 devices were isolated using lithography and selective wet etching. Concentrator grid geometries were used for the OMVPE-grown devices. The illuminated area was 0.100 cm^2, which excludes the bus bar area, while the total device area was 0.116 cm^2. Current density measured in the light was calculated using the illuminated area, while current density from measurements in the dark was calculated from the total area. The front GaAs or GaInNAs contact was removed via selective wet etching with the metal grids serving as a mask. A bilayer ZnS (45 nm)/MgF_2 (95 nm) anti-reflection coating was applied to the surface of the HVPE-grown devices via thermal evaporation. The post-processing device structure is shown in Figure 1A.

Solar cell characterization

External quantum efficiency was measured as a function of wavelength on a calibrated instrument using a white light source and a grating monochromator. *J-V* curves were measured from the devices in the dark and in the light under a simulated AM1.5G spectrum that used an XT-10 system with a variable height Xe-arc lamp. The lamp height was set using a GaAs reference cell fabricated and calibrated at NREL that was last calibrated and certified on 9/4/20. The spectral mismatch between the test devices and the reference was 0.5% or lower. Cells were measured in the open air at 25°C on a temperature-controlled vacuum hold-down stage. Cells were measured from forward to reverse bias in voltage increments of 5 mV. Dwell time was approximately 100 ms at each voltage. The *J-V* of the 27% efficiency HVPE-grown device was certified by the NREL's Cell and Module Performance (CMP) Team (see Figure S3). The CMP team's GaAs reference was last calibrated on 12/28/22. We present a comparison of the light *J-V* curve for this cell measured on our setup vs. the data from the independent certification team as of validation of the accuracy of our setup (Figure S4).

SUPPLEMENTAL INFORMATION

Supplemental information can be found online at https://doi.org/10.1016/j.xcrp.2023.101541.

ACKNOWLEDGMENTS

The authors gratefully acknowledge Waldo Olavarria and David Guiling for materials growth; Michelle Young, Evan W.K. Wong, and Zach Flagg for device processing;

and Sarah Collins for anti-reflection coating deposition. This work was authored by Alliance for Sustainable Energy, LLC, the Manager and Operator of the National Renewable Energy Laboratory for the US Department of Energy (DOE) under contract no. DE-AC36-08GO28308. This work was supported by the US Department of Defense under the Operational Energy Prototyping Fund (OEPF) from the Office of Operational Energy – Innovation. Additional support was provided by the DOE's Office of Energy Efficiency and Renewable Energy (EERE) under Solar Energy Technologies Office (SETO) Foundational Program to Accelerate Efficiency (F-PACE) agreement no. DE-EE00024619. The views expressed in the article do not necessarily represent the views of the DOE or the US Government.

AUTHOR CONTRIBUTIONS

Conceptualization, K.L.S., J.S., A.J.P., and M.A.S.; methodology, K.L.S.; investigation K.L.S., J.S., and M.A.S.; writing – original draft, K.L.S.; writing – review & editing, K.L.S., J.S., M.A.S., and A.J.P.; visualization, K.L.S. and J.S.; funding acquisition, A.J.P. and M.A.S.

DECLARATION OF INTERESTS

The authors declare no competing interests.

Received: May 9, 2023
Revised: June 29, 2023
Accepted: July 20, 2023
Published: August 24, 2023

REFERENCES

1. Geisz, J.F., Steiner, M.A., Garcia, I., Kurtz, S.R., and Friedman, D.J. (2013). Enhanced external radiative efficiency for 20.8% efficient single-junction GaInP solar cells. Appl. Phys. Lett. *103*, 041118. https://doi.org/10.1063/1.4816837.

2. Hwang, S.-T., Kim, S., Cheun, H., Lee, H., Lee, B., Hwang, T., Lee, S., Yoon, W., Lee, H.-M., and Park, B. (2016). Bandgap grading and $Al_{0.3}Ga_{0.7}As$ heterojunction emitter for highly efficient GaAs-based solar cells. Sol. Energy Mater. Sol. Cell. *155*, 264–272. https://doi.org/10.1016/j.solmat.2016.06.009.

3. Ragay, F., Ruigrok, E., and Wolter, J. (1994). GaAs-AlGaAs heterojunction solar cells with increased open-circuit voltage. Proceedings of 1994 IEEE 1st World Conference on Photovoltaic Energy Conversion *2*, 1934–1937. https://doi.org/10.1109/WCPEC.1994.520747.

4. Sah, C.-T., Noyce, R., and Shockley, W. (1957). Carrier generation and recombination in pn junctions and pn junction characteristics. Proc. IRE *45*, 1228–1243. https://doi.org/10.1109/JRPROC.1957.278528.

5. Sun, Y., Perna, A., and Bermel, P. (2019). Comparing Front-and Rear-Junction GaInP Photovoltaic Devices Through Detailed Numerical and Analytical Modeling. IEEE J. Photovoltaics *9*, 437–445. https://doi.org/10.1109/JPHOTOV.2019.2892530.

6. Nakamura, T., Yanwachirakul, W., Imaizumi, M., Sugiyama, M., Akiyama, H., and Okada, Y. (2021). Reducing Shockley–Read–Hall recombination losses in the depletion region of a solar cell by using a wide-gap emitter layer. J. Appl. Phys. *130*, 153102. https://doi.org/10.1063/5.0060158.

7. Steiner, M., Geisz, J., Garcia, I., Friedman, D., Duda, A., and Kurtz, S. (2013). Optical enhancement of the open-circuit voltage in high quality GaAs solar cells. J. Appl. Phys. *113*, 123109. https://doi.org/10.1063/1.4798267.

8. Helmers, H., Lopez, E., Höhn, O., Lackner, D., Schön, J., Schauerte, M., Schachtner, M., Dimroth, F., and Bett, A.W. (2021). 68.9% efficient GaAs-based photonic power conversion enabled by photon recycling and optical resonance. Phys. Status Solidi RRL *15*, 2100113. https://doi.org/10.1002/pssr.202100113.

9. Pauwels, H.J., and Vanhoutte, G. (1978). The influence of interface state and energy barriers on the efficiency of heterojunction solar cells. J. Phys. D Appl. Phys. *11*, 649–667. https://doi.org/10.1088/0022-3727/11/5/009.

10. Olson, J., Steiner, M., and Kanevce, A. (2011). Using measurements of fill factor at high irradiance to deduce heterobarrier band offsets. In Proceedings of the 37th Photovoltaic Specialists Conference, pp. 003754–003757. https://doi.org/10.1109/PVSC.2011.6186459.

11. Varache, R., Leendertz, C., Gueunier-Farret, M., Haschke, J., Muñoz, D., and Korte, L. (2015). Investigation of selective junctions using a newly developed tunnel current model for solar cell applications. Sol. Energy Mater. Sol. Cell. *141*, 14–23. https://doi.org/10.1016/j.solmat.2015.05.014.

12. Simon, J., Schulte, K., Horowitz, K., Remo, T., Young, D., and Ptak, A. (2018). III-V-Based Optoelectronics with Low-Cost Dynamic Hydride Vapor Phase Epitaxy. Crystals *9*, 3. https://doi.org/10.3390/cryst9010003.

13. Shoji, Y., Oshima, R., Makita, K., Ubukata, A., and Sugaya, T. (2022). 28.3% Efficient III–V Tandem Solar Cells Fabricated Using a Triple-Chamber Hydride Vapor Phase Epitaxy System. Solar RRL *6*, 2100948. https://doi.org/10.1002/solr.202100948.

14. De Wolf, S., Descoeudres, A., Holman, Z.C., and Ballif, C. (2012). High-efficiency silicon heterojunction solar cells: A review. Green *2*, 7–24. https://doi.org/10.1515/green-2011-0018.

15. Kumar, S.G., and Rao, K.S.R.K. (2014). Physics and chemistry of CdTe/CdS thin film heterojunction photovoltaic devices: fundamental and critical aspects. Energy Environ. Sci. *7*, 45–102. https://doi.org/10.1039/C3EE41981A.

16. Hu, Y., Schlipf, J., Wussler, M., Petrus, M.L., Jaegermann, W., Bein, T., Müller-Buschbaum, P., and Docampo, P. (2016). Hybrid perovskite/perovskite heterojunction solar cells. ACS Nano *10*, 5999–6007. https://doi.org/10.1021/acsnano.6b01535.

17. Zhang, Y., Mascarenhas, A., and Wang, L.-W. (2002). Band alignment between GaAs and partially ordered GaInP. Appl. Phys. Lett. *80*, 3111–3113. https://doi.org/10.1063/1.1472478.

18. Cho, Y.H., Kim, K.S., Ryu, S.W., Kim, S.K., Choe, B.D., and Lim, H. (1995). Determination of the

conduction-band discontinuities of $In_{0.5}Ga_{0.5}P/In_{1-x}GaxAs_{1-y}P_y$ by capacitance–voltage analysis. Appl. Phys. Lett. *66*, 1785–1787. https://doi.org/10.1063/1.113321.

19. Hinojosa, M., García, I., Dadgostar, S., and Algora, C. (2021). Point-defects assisted Zn-diffusion in AlGaInP/GaInP systems during the MOVPE growth of inverted multijunction solar cells. IEEE J. Photovoltaics *11*, 429–436. https://doi.org/10.1109/JPHOTOV.2020.3043849.

20. Geisz, J.F., Steiner, M.A., García, I., France, R.M., McMahon, W.E., Osterwald, C.R., and Friedman, D.J. (2015). Generalized optoelectronic model of series-connected multijunction solar cells. IEEE J. Photovoltaics *5*, 1827–1839. https://doi.org/10.1109/JPHOTOV.2015.2478072.

21. Lindholm, F.A., Fossum, J.G., and Burgess, E.L. (1979). Application of the superposition principle to solar-cell analysis. IEEE Trans. Electron. Dev. *26*, 165–171. https://doi.org/10.1109/T-ED.1979.19400.

22. Lee, J.-K., Cho, Y.-H., Choe, B.-D., Kim, K.S., Jeon, H.I., Lim, H., and Razeghi, M. (1997). Schottky barrier heights and conduction-band offsets of $In_{1-x}Ga_xAs_{1-y}P_y$ lattice matched to GaAs. Appl. Phys. Lett. *71*, 912–914. https://doi.org/10.1063/1.119686.

23. Metaferia, W., Schulte, K.L., Simon, J., Johnston, S., and Ptak, A.J. (2019). Gallium arsenide solar cells grown at rates exceeding 300 μm h^{-1} by hydride vapor phase epitaxy. Nat. Commun. *10*, 3361. https://doi.org/10.1038/s41467-019-11341-3.

24. Boyer, J.T., Schulte, K.L., Young, M.R., Ptak, A.J., and Simon, J. (2023). AlInP-passivated III–V solar cells grown by dynamic hydride vapor-phase epitaxy. Progress in Photovoltaics. *31*, 230–236. https://doi.org/10.1002/pip.3629.

25. Jain, N., Simon, J., Schulte, K.L., Friedman, D.J., Diercks, D.R., Packard, C.E., Young, D.L., and Ptak, A.J. (2018). Tunable Bandgap GaInAsP Solar Cells With 18.7% Photoconversion Efficiency Synthesized by Low-Cost and High-Growth Rate Hydride Vapor Phase Epitaxy. IEEE J. Photovoltaics *8*, 1577–1583. https://doi.org/10.1109/JPHOTOV.2018.2865172.

26. Heckelmann, S., Lackner, D., Dimroth, F., and Bett, A. (2017). Material quality frontiers of MOVPE grown AlGaAs for minority carrier devices. J. Cryst. Growth *464*, 49–53. https://doi.org/10.1016/j.jcrysgro.2016.09.069.

27. Batey, J., and Wright, S.L. (1986). Energy band alignment in GaAs:(Al, Ga) As heterostructures: The dependence on alloy composition. J. Appl. Phys. *59*, 200–209. https://doi.org/10.1063/1.336864.

28. Wang, W. (1986). On the band offsets of AlGaAs/GaAs and beyond. Solid State Electron. *29*, 133–139. https://doi.org/10.1016/0038-1101(86)90031-6.

29. Levinshtein, M.E., and Rumyantsev, S.L. (1997). Gallium Arsenide (World Scientific).

30. Goldberg, Y.A. (1997). Gallium Indium Phosphide (World Scientific).

31. Goldberg, Y.A. (1997). Aluminium Gallium Arsenide (World Scientific).

32. Martín, G., Coll, C., López-Conesa, L., Rebled, J.M., Barrigón, E., García, I., Rey-Stolle, I., Algora, C., Cornet, A., Estradé, S., and Peiró, F. (2022). Understanding the Anisotropy in the Electrical Conductivity of CuPtB-type Ordered GaInP Thin Films by Combining In Situ TEM Biasing and First Principles Calculations. ACS Appl. Electron. Mater. *4*, 3478–3485. https://doi.org/10.1021/acsaelm.2c00415.

33. Ahrenkiel, R.K., Keyes, B.M., Lush, G.B., Melloch, M.R., Lundstrom, M.S., and MacMillan, H.F. (1992). Minority-carrier lifetime and photon recycling in n-GaAs. J. Vac. Sci. Technol. A: Vacuum, Surfaces, and Films *10*, 990–995. https://doi.org/10.1116/1.577892.

34. Steiner, M.A., Geisz, J.F., Garcia, I., Friedman, D.J., Duda, A., Olavarria, W.J., Young, M., Kuciauskas, D., and Kurtz, S.R. (2013). Effects of Internal Luminescence and Internal Optics on V_{OC} J_{SC} of III–V Solar Cells. IEEE J. Photovoltaics *3*, 1437–1442. https://doi.org/10.1109/JPHOTOV.2013.2278666.

35. Martin, G.M., Mitonneau, A., and Mircea, A. (1977). Electron traps in bulk and epitaxial GaAs crystals. Electron. Lett. *13*, 191–193.

36. Samuelson, L., Titze, P., and Grimmeiss, H.G. (1981). Electrical and optical properties of deep levels in MOVPE grown GaAs. J. Cryst. Growth *55*, 164–172. https://doi.org/10.1016/0022-0248(81)90284-0.

37. Matsumoto, T., Bhattacharya, P.K., and Ludowise, M.J. (1982). Behavior of the 0.82 eV and other dominant electron traps in organometallic vapor phase epitaxial $Al_xGa_{1-x}As$. Appl. Phys. Lett. *41*, 662–664. https://doi.org/10.1063/1.93605.

38. Hashizume, T., Hasegawa, H., and Ohno, H. (1990). Midgap states in metalorganic vapor phase epitaxy grown $Al_xGa_{1-x}As$. J. Appl. Phys. *68*, 3394–3400. https://doi.org/10.1063/1.346344.

39. Feng, S.L., Bourgoin, J.C., Omnes, F., and Razeghi, M. (1991). Defects in organometallic vapor-phase epitaxy-grown GaInP layers. Appl. Phys. Lett. *59*, 941–943. https://doi.org/10.1063/1.106308.

40. Kim, J.H., Jo, S.J., Kim, J.W., and Song, J.-I. (2001). Characterization of deep levels in InGaP grown by compound-source molecular beam epitaxy. J. Appl. Phys. *89*, 4407–4409. https://doi.org/10.1063/1.1353559.

41. Jakomin, R., Parisini, A., Tarricone, L., Longo, M., Fraboni, B., and Vantaggio, S. (2012). On the electrical properties of Si-doped InGaP layers grown by low pressure-metalorganic vapor phase epitaxy. Thin Solid Films *520*, 6619–6625. https://doi.org/10.1016/j.tsf.2012.07.009.

42. Mitonneau, A., Mircea, A., Martin, G., and Pons, D. (1979). Electron and hole capture cross-sections at deep centers in gallium arsenide. Rev. Phys. Appl. *14*, 853–861.

43. Bonilla, L.L., Hernando, P.J., Kindelan, M., and Piazza, F. (1999). Determination of EL2 capture and emission coefficients in semi-insulating n-GaAs. Appl. Phys. Lett. *74*, 988–990.

44. Prinz, V.Ya., and Rechkunov, S.N. (1983). nfluence of a Strong Electric Field on the Carrier Capture by Nonradiative Deep-Level Centers in GaAs. Physica status solidi (b) *118*, 159–166.